

# HOW DO TIDES AFFECT UNDERWATER ACOUSTIC PROPAGATION?

## A COLLABORATIVE APPROACH TO IMPROVE INTERNAL WAVE MODELING AT BASIN TO GLOBAL SCALES

By Martha C. Schönau, Luna Hiron, John Ragland, Keshav J. Raja, Joseph Skitka, Miguel S. Solano, Xiaobiao Xu, Brian K. Arbic, Maarten C. Buijsman, Eric P. Chassignet, Emanuel Coelho, Robert W. Helber, William Peria, Jay F. Shriver, Jason E. Summers, Kathryn L. Verlinden, and Alan J. Wallcraft

**ABSTRACT.** Accurate prediction of underwater sound speed and acoustic propagation is dependent on realistic representation of the ocean state and its underlying dynamics within ocean models. Stratified, high-resolution global ocean models that include tidal forcing better capture the ocean state by introducing internal tides that generate higher frequency (supertidal) internal waves. Through the disciplines of internal wave modeling, acoustics, and machine learning, we examined how internal wave energy moves through numerical simulations, how this energy alters the ocean state and sound speed, and how machine learning could aid the modeling of these impacts. The project used global, basin-scale, and idealized HYbrid Coordinate Ocean Model (HYCOM) simulations as well as regional Massachusetts Institute of Technology general circulation model (MITgcm) simulations to examine how tidal inclusion affects sea surface height variability, the propagation and dissipation of internal wave energy, and the sensitivity of internal wave modeling to vertical and horizontal grid spacing. Sound speed, acoustic parameters, and modeled acoustic propagation were compared between simulations with and without tidal forcing, and deep learning algorithms were used to examine how a tidally forced ocean state could be generated while reducing computational costs.

### INTRODUCTION

The underwater soundscape encompasses a range of ambient, anthropogenic, and biological sound, with research spanning acoustic communications to passive acoustic monitoring. The density of water allows sound, which is a pressure wave, to travel short distances and across ocean basins. The speed of sound is set by water temperature and salinity, and pressure. As it travels, sound scatters from the bathymetry, the surface, animals, or other objects. Sound refracts when it encounters a difference in sound speed, which can be introduced by fronts, eddies, currents, vertical stratification, internal tides, and gravity waves and mixing.

Soundscape modeling, such as that used to trace the impacts of anthropogenic noise on marine mammals, is dependent on the sound speed structure employed in the ocean model. The vertical motions of internal tides and internal gravity waves (IGWs) bring cold water up and push warm water down, changing the sound speed (Gill, 1982). Internal tides and IGWs dissipate energy to both smaller and larger scales. The sound speed in tidally forced simulations may differ drastically from simulations without tidal forcing. Simulations are also highly sensitive to grid spacing, mixing parameterizations, and boundary conditions. Identifying the differences of tidally driven ocean models

from their non-tidal counterparts and the actual ocean, and the length scales that resolve IGW processes, may in turn inform how internal wave models should be used for diverse acoustic and biological studies.

This paper presents progress in the modeling of internal tides and IGWs, the effect of these advances on modeling sound speed and sound propagation in underwater ray-tracing acoustic models, and the use of deep learning (DL) to predict the ocean state. The research stems from a coordinated project funded under the Office of Naval Research (ONR) Task Force Ocean (TFO) initiative designed to train early career scientists in cross-disciplinary oceanography, underwater acoustics, and machine learning techniques. The project was dubbed “TFO-HYCOM” after the US Navy’s operational HYbrid Coordinate Ocean Model (HYCOM), which featured prominently in the research project.

### BACKGROUND AND APPROACH

#### Internal Gravity Waves

Internal gravity waves exist as undulations along constant density ocean surfaces (isopycnals) with a restoring force of gravity. As IGWs displace isopycnals, they create a profile of depth-dependent velocities. Internal tides, a special type of IGWs, exist at tidal frequencies and are generated by tidal flow over

bathymetric features (e.g., Bell, 1975). They differ from near-inertial IGWs that are generated by high-frequency wind forcing that have frequencies near the Coriolis frequency (Pollard and Millard, 1970). Aside from internal tides and near-inertial waves, there is a spread of internal wave energy known as the IGW continuum spectrum (Garrett and Munk, 1975), which can be shaped by mesoscale eddies (Barkan et al., 2017) and nonlinear interactions. Nonlinear interactions can bring IGW scales down to 1 m or less and can cause IGWs to overturn and break, a dominant process in the mixing of the ocean interior (MacKinnon et al., 2017).

IGWs can be discussed in terms of their vertical structures, or “modes” (Gill, 1982). These modes approximate IGW dynamics as a linear superposition of standing waves in the vertical direction and propagating waves in the horizontal direction. This is reasonable in a buoyancy-driven flow where the horizontal scale is much greater than that of the vertical. Each wave mode has a characteristic length, phase speed, and vertical structure that depends on the frequency of the IGW, the Coriolis frequency, and the vertical density gradient. The lowest baroclinic mode has a singular, two-layer horizontal structure (i.e., the velocities are out of phase above and below the thermocline); higher modes have greater vertical structure. Waves in the IGW spectrum at frequencies greater than tidal frequency, called super-tidal, are thought to arise from nonlinear interactions between internal tides and near-inertial IGWs (Müller et al., 1986).

IGW variability has not been well captured by global ocean simulations. Simulations may lack certain forcing (e.g., tidal) or may parameterize, rather than resolve, finer-scale processes. Barotropic tidal models, where water movement is uniform with depth, have been available since the 1970s (e.g., Hendershott, 1981), but they do not allow stratified flow. In the last two decades, increases in computational power have made it possible to accurately model internal tides in a stratified ocean. These models have evolved from using horizontally uniform two-layer (Arbic et al., 2004) or multilayer (Simmons et al., 2004) stratification to embedding tidal forcing in ocean general circulation simulations with stratification that varies geographically in a realistic manner (Arbic et al., 2012).

This study focused on the modeling of internal tides and IGWs in HYCOM, the backbone of the operational forecasting system of the US Navy (Metzger et al., 2014). The Navy HYCOM simulations use a hybrid vertical coordinate system: isopycnal coordinates in the stratified ocean interior, a dynamic transition to pressure ( $p$ ) coordinates in the surface mixed layer, and bathymetry-following ( $\sigma$ ) coordinates in shallow shelf water (Bleck, 2002; Chassignet et al., 2006). The simulations use realistic atmospheric forcing from the Navy Global Environmental Model (NAVGENM; Hogan et al., 2014) and can be run with or without data assimilation and with or without tidal forcing. Sophisticated methods from the data-assimilation literature have also been applied to bring the tidal simulations closer to

observations (Ngodock et al., 2016).

For this study, HYCOM was primarily utilized without data assimilation. Data assimilation can create “shocks” as it brings the model closer to observations, disrupting the geostrophic balance between horizontal pressure gradients and rotation. Raja et al. (2024) found that as the modeled ocean tries to restore geostrophic balance, spurious low-mode internal waves are generated. These waves have frequencies that overlap with the tidal and inertial bands, complicating the analysis of naturally occurring tidal and near-inertial waves. The interaction of these spurious IGWs with other internal waves or eddies and their eventual dissipation can also alter the ocean energetics. For this reason, most of our HYCOM internal tide and IGW studies (e.g., Raja et al., 2022), and subsequent acoustics research for this project, have used HYCOM simulations without data assimilation.

The HYCOM model was used in this study with a variety of vertical, horizontal, and bathymetric grid spacings. The most-used model setups were regional and global versions of tidally forced HYCOM with a horizontal grid spacing of  $1/25^\circ$  to  $1/50^\circ$ , typically the highest resolution spacing at which Global HYCOM can be run. This is finer than the  $1/12^\circ$  grid spacing available in most of today’s publicly available global ocean models. Idealized versions of the model, such as using a single temperature-salinity profile in a two-dimensional field, were used to isolate the effects of internal tides on stratification and energy transfer. Regional simulations using the Massachusetts Institute of Technology general circulation model (MITgcm) were compared to HYCOM simulations because of MITgcm’s different boundary conditions and, for this study, its finer grid spacing.

## Sound Propagation

Internal tides and IGWs have long been associated with underwater acoustics. The influence of internal tides and IGWs on sound speed variability has been at the core of many observational (e.g., Flatté et al., 1979; Tang et al. 2007; Worcester et al., 2013) and modeling (e.g., Colosi and Flatté, 1996) studies. Alternatively, acoustic tomography, an inverse method that uses long-range acoustic propagations to infer ocean structure, has been used to study the barotropic and baroclinic tides themselves (Dushaw, 2022). In addition to the tilt of density surfaces caused by internal waves, temperature and salinity fluctuations along a constant density surface, called “spice,” can have a similarly large impact on sound speed and its gradients (Dzieciuch et al., 2004). “Spiciness,” caused by ocean stirring by mesoscale eddies, could differ between tidal and non-tidally forced ocean simulations.

This study focused on upper ocean acoustic structure and propagation. In the uniform temperature and salinity layer found at the ocean surface in many regions, pressure causes sound speed to increase with depth, often creating a local subsurface maximum in sound speed (Helber et al., 2008). This subsurface sound-speed maximum, called the sonic layer depth (SLD), has the potential to form a surface-layer duct where sound is

refracted upward from the SLD and reflected downward by the surface, allowing acoustic energy to travel long distances. The sound speed gradient below the SLD, called the below-layer gradient (BLG), can influence the potential of this surface-layer duct to trap energy.

For this project, sound speed, its variability, the SLD, and the BLG were compared between simulations with and without tidal forcing. Acoustic transmission loss (TL), an estimate of acoustic pressure, was calculated from a virtual source using a three-dimensional ray-tracing acoustic model, Bellhop 3D (Porter, 2011). TL exemplifies how the differences in sound speed between differently forced ocean simulations can affect acoustic propagation models.

## PROGRESS IN IGW MODELING

### Bringing Models Closer to Observations

Realistically capturing ocean variability at different length scales, from large-scale eddies to smaller coastal features, is a central goal of global ocean models. Sea surface height (SSH) variability is a useful proxy for mesoscale ocean variability. The SSH wavenumber spectrum was used as a single descriptor of the relative strength of ocean variability as a function of length scale. Wavenumber, defined as one divided by wavelength, is large where spatial scales are small. **Figure 1f** shows an example of the wavenumber spectra and the spectral slope of the mesoscale

variability (the steepness of the spectrum from 250 km to 70 km wavelength). The SSH spectral slope varies greatly by location (**Figure 1e**; Zhou et al., 2015). The slope is steepest ( $-5$ ) along the western boundary current (Gulf Stream), which has large-scale currents and high mesoscale eddy variability. The slopes are flatter (close to  $-3$ ) in the mid-latitude interior, such as the eastern North Atlantic, and much flatter (close to  $-1$ ) in the equatorial region.

The inclusion of tidal forcing in ocean models is paramount to bringing SSH variability in simulations closer to observations. **Figure 1** compares a series of high-resolution regional  $1/50^\circ$  North Atlantic HYCOM simulations to satellite altimetry observations. Without tidal forcing, high-resolution models could not replicate this spatial SSH variability (e.g., **Figure 1a,b**; Chassignet and Xu, 2017). With tidal forcing (**Figure 1c,d**), the SSH spectral slope in the equatorial Atlantic and the eastern subtropical North Atlantic began to match observations. Here, there are strong barotropic tides and strong stratification in the upper layer of the water column. In these regions, SSH variability at length scales of 70–120 km increased, flattening the spectral slope in the 70–250 km mesoscale range (**Figure 1f**). High-resolution bathymetry (**Figure 1b**) and high-frequency wind variability (Figure 7b in Xu et al., 2022) had comparably minor impacts on the spectral slope, except at local scales where internal tides are generated along topography, such as near the shelf break (Xu et al., 2022).

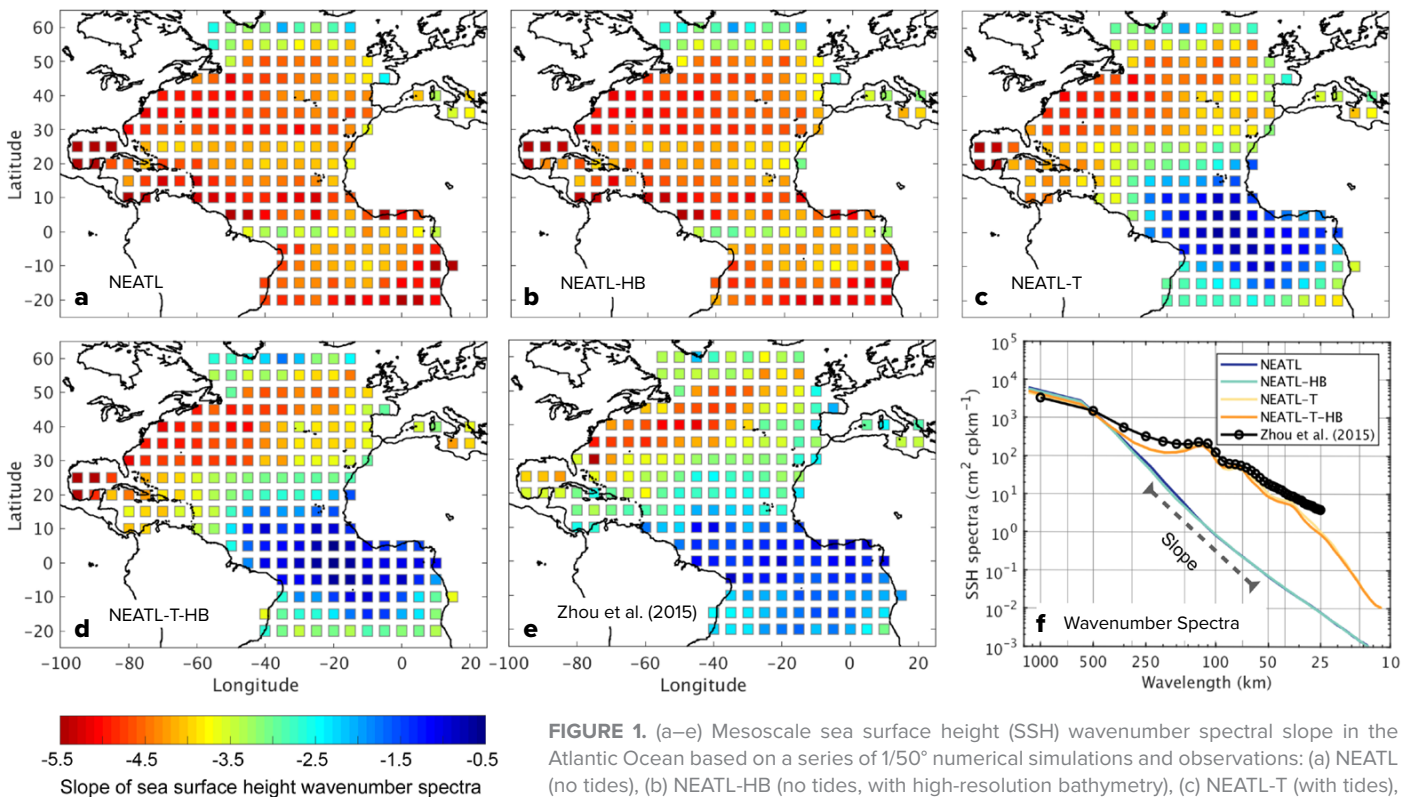


**FIGURE 1.** (a–e) Mesoscale sea surface height (SSH) wavenumber spectral slope in the Atlantic Ocean based on a series of  $1/50^\circ$  numerical simulations and observations: (a) NEATL (no tides), (b) NEATL-HB (no tides, with high-resolution bathymetry), (c) NEATL-T (with tides), (d) NEATL-T-HB (with tides, high-resolution bathymetry), and (e) satellite observations from Zhou et al. (2015). (f) Example of the wavenumber spectra averaged from  $10^\circ\text{S}$ – $10^\circ\text{N}$  and  $35^\circ$ – $15^\circ\text{W}$  from observations and four model configurations. The mesoscale spectral slope in panels a–e was calculated between 70 km and 250 km. Modified from Xu et al. (2022; their Figures 7 and 11)

### From Global to Regional: Supertidal Energy

Tidal energy is mainly concentrated at the diurnal and semi-diurnal astronomical forcing frequencies, and some of this energy is transferred to higher (and lower) frequencies. Band-pass filtering can separate the energy between that at semi-diurnal tidal frequencies (Figure 2a) and that at higher, supertidal frequencies (Figure 2b). Diurnal and semidiurnal energy dominate most of the internal tide spectrum, except along the path of large amplitude internal tides near the equator. Most of the research on IGW-IGW interactions in the open ocean has focused on “subharmonic resonance,” a transfer of tidal energy to lower frequencies (e.g., Ansong et al., 2018). For this project, Solano et al. (2023) evaluated the decay of the low-mode internal tide due to superharmonic wave-wave interactions, leading to the transfer of tidal energy to higher, supertidal frequencies. Globally, supertidal kinetic energy (KE) accounts for about 5%

of the total IGW energy. Supertidal energy is greatest at low latitudes. Equatorward of 25°, 9% of the total tidal energy is transferred to supertidal KE. At generation sites of large amplitude internal tides or “hotspots,” such as the Bay of Bengal, the Amazon Shelf, and the Mascarene Ridge, 25%–50% of the IGW KE is found at supertidal frequencies (Solano et al., 2023; Buijsman et al., 2025).

Here, we focus on two regions with high supertidal KE: the Amazon Shelf and the Mascarene Ridge (Figure 3). The nonlinear IGW KE transfer from primary to supertidal frequencies has a banding pattern (Figure 3a,b) that is also present in the horizontal divergence of the supertidal energy flux (Figure 3c,d), suggesting a common mechanism for the nonlinear energy transfer between length scales. Decomposing the energy into separate modes (Figure 3e,f), the banding pattern appears when the lowest modes (1+2) are superimposed but not for individual modes.

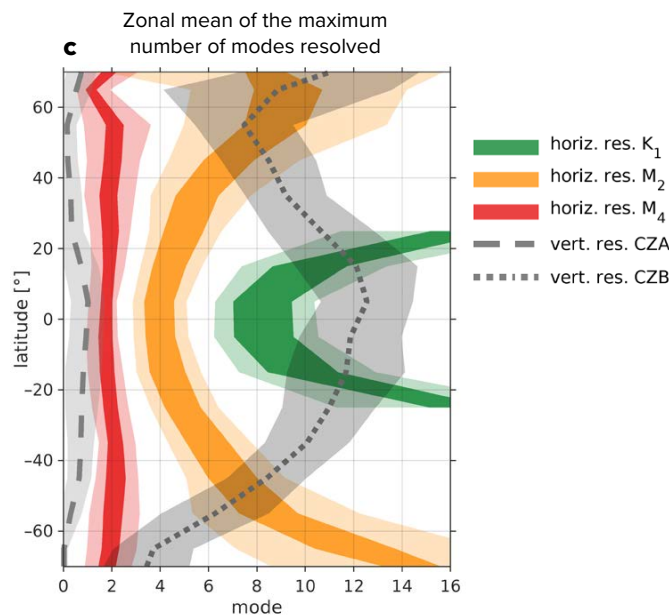
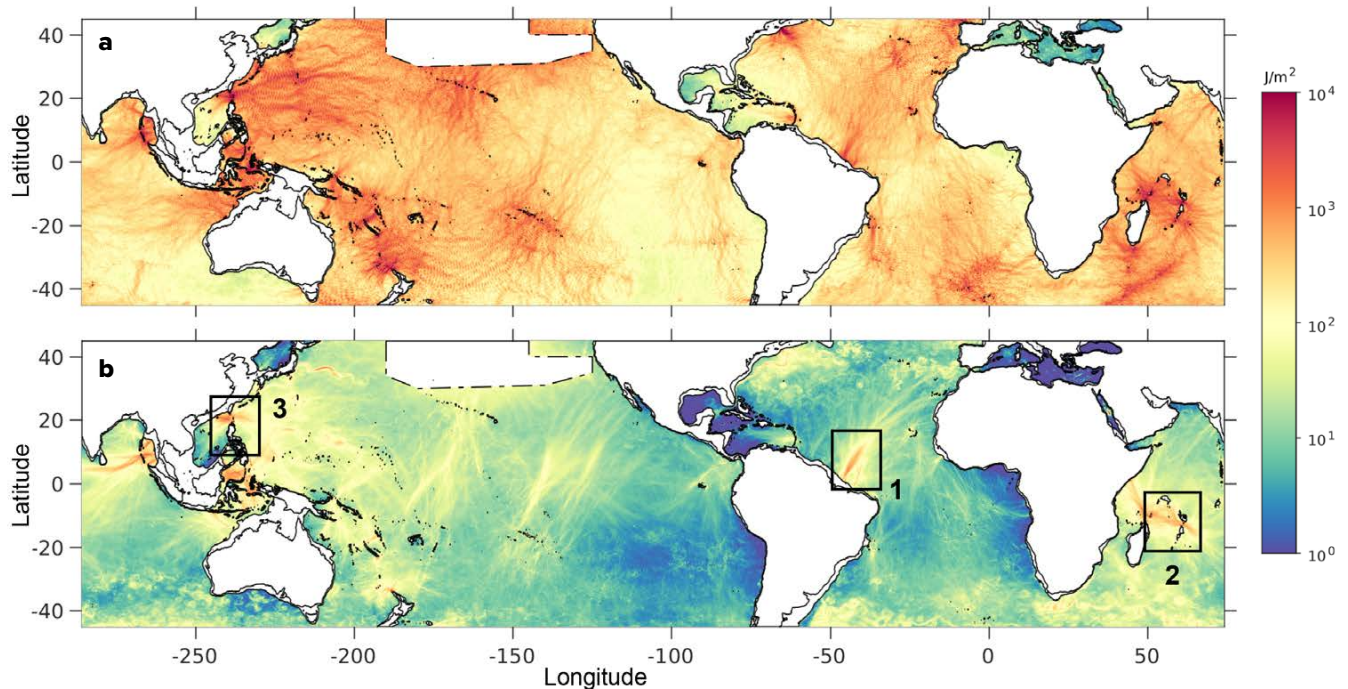


**FIGURE 2.** Time-mean and depth-integrated internal wave kinetic energy ( $J m^{-2}$ ) band-passed at (a) semidiurnal, and (b) supertidal frequencies. Regions with relatively high supertidal energy indicated by the black rectangles are: (1) the Amazon Shelf, (2) the Mascarene Ridge, and (3) the Luzon Strait. (c) Zonal mean (averaged over seafloor depths  $>2,000$  m and  $10^\circ$  latitude bins) of the maximum number of modes (vertical structures) resolved for various internal tide frequency resolution criteria.  $K_1$ ,  $M_2$ ,  $M_4$  represent the dominant diurnal, semidiurnal, and supertidal constituents of internal tides with decreasing wavelengths, respectively. For the horizontal (vertical) resolution, the dark-colored polygons (dashed lines) mark the range of the number of resolved modes for the zonal mean, and the light-colored polygons  $\pm 1$  standard deviation from this mean.

Thus, it is likely that the mode-1 and mode-2 internal tides interfere constructively at the locations of the patches where their velocities are in phase and increase the tidal amplitude, steepen the internal tide, and enhance the energy transfer to higher harmonics. The locations of these patches are modulated by the slowly varying subtidal current and the spring-neap cycle, with greater energy available to transfer to higher-harmonics during spring tides (Solano et al., 2023).

### Impacts of Horizontal and Vertical Grid Spacing on IGWs in Global Models

Ocean model grid spacing, both horizontal and vertical, determines how bathymetry and the wavelengths of IGW modes are resolved. For example, a decrease in HYCOM horizontal grid size from 8 km to 4 km can increase the IGW generation and energy density by about 50%, largely because it increases the number of internal wave modes resolved (Buijsman et al., 2020).

We examined what diurnal, semidiurnal, and supertidal vertical wave modes could be resolved in a global,  $1/25^\circ$  tidally forced global HYCOM simulation with 41 layers (Figure 2c). Horizontal spacing and IGW wavelengths vary spatially in global ocean models. Earth's sphericity causes grid spacing to decrease

poleward, while wavelengths of tidally generated IGWs increase poleward with the increase of the Coriolis frequency (Buijsman et al., 2025). We used the criterion that a vertical mode could be resolved if there were at least six to eight horizontal grid spacings per wavelength (Stewart et al., 2017). A similar criterion was applied for the vertical resolution, called vertical criterion CZA. However, this criterion was designed for  $z$ -coordinate models, whereas HYCOM is an isopycnal model below the mixed layer. Therefore, an additional criterion was developed to account for the changes in vertical and horizontal velocity structure caused by isopycnals, called vertical criterion CZB.

In the horizontal, internal wave modes with lower frequencies (longer wavelength) were better resolved. For example,  $K_1$  had eight modes resolved at the equator and 20 modes near the  $K_1$  turning latitude of about  $30^\circ$  (Figure 2c). (Poleward of this latitude, the tidal frequency is lower than the Coriolis frequency, and diurnal IGWs cannot exist.) The shorter wavelength,  $M_2$ , had fewer modes resolved, with only about four modes resolved at the equator. For supertidal waves,  $M_4$ , which has the most energy globally (Buijsman et al., 2025), only two modes were resolved. The number of resolved modes was sensitive to the vertical resolution criteria. CZB appeared to be a more appropriate

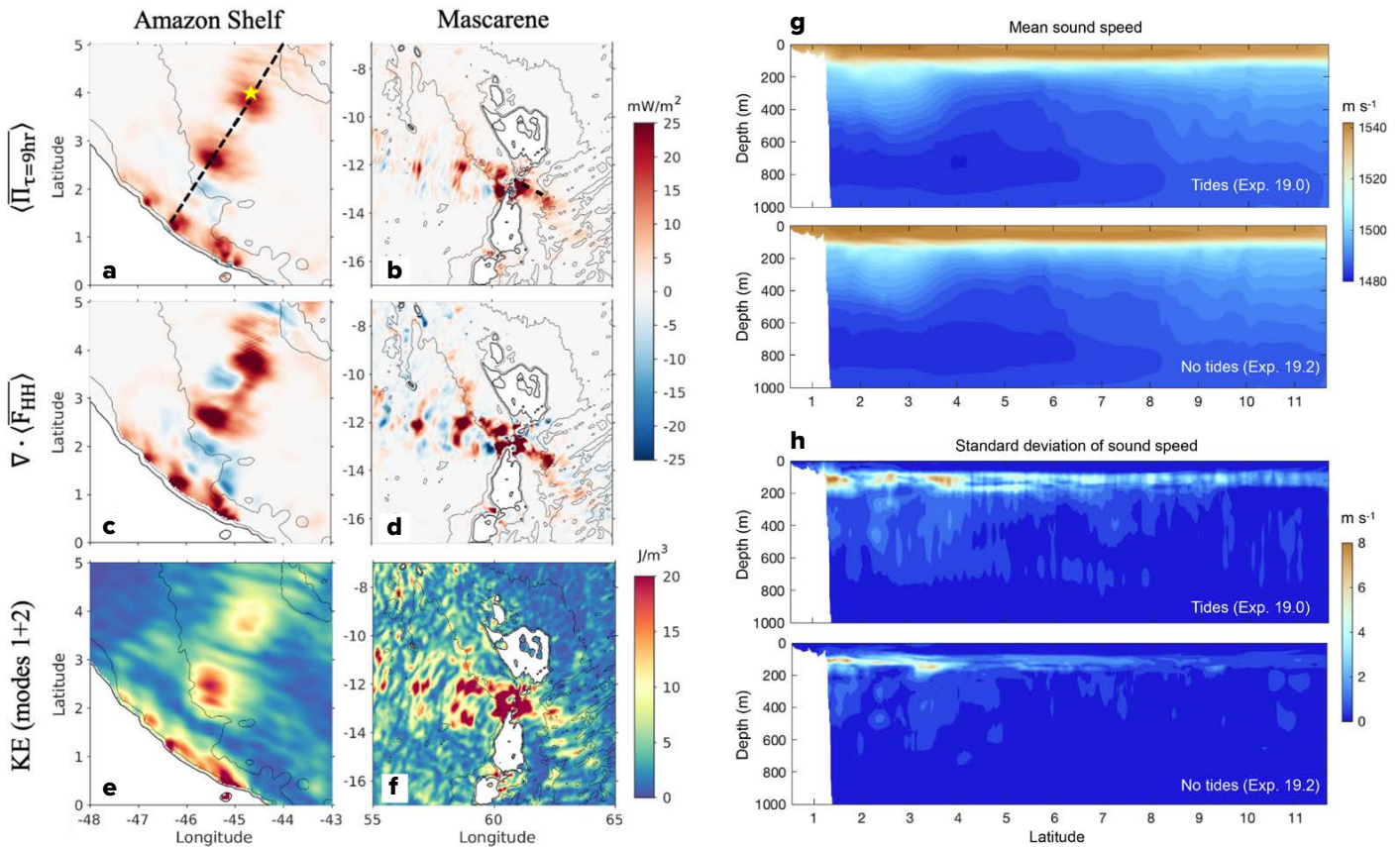


**FIGURE 3.** At the Amazon Shelf and the Mascarene Ridge: (a,b) time-mean and depth-integrated kinetic energy transfer  $\langle \Pi_{(T=9hr)} \rangle$ ; (c,d) time-mean, depth-integrated divergence of supertidal energy flux  $\nabla \cdot \langle F_{HH} \rangle$ ; (e,f) time-mean surface kinetic energy (KE) for the superposition of modes 1 and 2. Panels (a–f) were modified from Solano et al. (2023). (g) Mean sound speed and (h) standard deviation of sound speed for each the tidally and non-tidally forced HYCOM simulations from May 20–29, 2019, in the Amazon region, plotted by latitude along the dotted line shown in (a). The star and radial (dashed black line) in (a) are noted for reference in Figure 6. In (b), a short, dashed line indicates the transect used in Figure 5b,c.

criterion than CZA. Accounting for the isopycnal layering in HYCOM, as in CZB, a maximum of 12 diurnal modes could be resolved at the equator.

### Vertical Grid Spacing in Idealized Models

Recent discussions among the oceanography community resolve that global models can achieve a more accurate ocean state if they include tidal forcing and have a horizontal grid spacing on the order of  $1/50^\circ$  or finer (the most up-to-date global HYCOM has  $1/25^\circ$  grid spacing). However, the optimal number of vertical layers needed in submesoscale resolving models to resolve internal tides and their energetics is unknown. To explore this question, we used an idealized HYCOM configuration with  $1/100^\circ$  horizontal grid spacing ( $\sim 1$  km), forced only by the semidiurnal ( $M_2$ ) tides over a centrally spaced ridge, and varied the number of layers in the simulations from 8 to 128 (Figure 4; Hiron et al., 2025). The idealized configuration allowed the problem to be isolated from contamination by ocean eddies and currents while resolving all the physics allowed in HYCOM.

Each idealized simulation was initialized with a climatological temperature profile averaged over the Cape Verde area and constant salinity. The domain size, approximately 8,000 km in the zonal direction, was large enough to prevent the reflection of internal tides at the boundaries. The vertical grid discretization was chosen based on characteristic wavelengths of different IGW modes. To generate internal tides, a steep ridge with a Gaussian shape was added in the center of the domain. The criticality of the slope, which is a measure of the ridge steepness normalized by the ray slope of the internal waves, was larger than one, allowing for nonlinear waves and wave beams to be

generated (Garrett and Kunze, 2007).

The wave beams were the strongest near the ridge (Figure 4a). The depth-integrated vertical KE of the 8- and 16-layer simulations differed from the others in amplitude and phase (Figure 4b). As the number of layers increased, the simulations became more similar. For the 48- to the 128-layer simulations, amplitude and phase were similar across simulations. When integrated from 0–2,000 m, the tidal barotropic-to-baroclinic energy conversion, the vertical kinetic energy, and the turbulent dissipation were greatest in the 128-layer simulation and decreased with coarser vertical grid spacing (Hiron et al., 2025). These variables converged for the simulations with greater than 48 layers, showing that the number of vertical layers can determine the IGW energy transfer; however, these results may differ at other horizontal grid spacings.

### A Final Word on Grid Spacing: Interaction of IGWs and Eddies

The IGW spectrum covers the transfer of energy between IGWs and the transfer of KE from its injection at large scales in eddies, near-inertial waves, and tides to the smallest scales. It is applicable globally but uses free parameters to account for regional and seasonal variations of the ocean state, such as the slowly varying background circulation and surface forcing. Ongoing research focuses on what determines these parameters and any deviation from this spectral form; nonlinear interactions involving IGWs, such as those on display in the Amazon basin and near Mascarene Ridge, are thought to be of particular importance.

Previous work on IGW-IGW interactions has identified some important processes that move energy to smaller scales (McComas and Bretherton, 1977; Dematteis et al., 2022). These

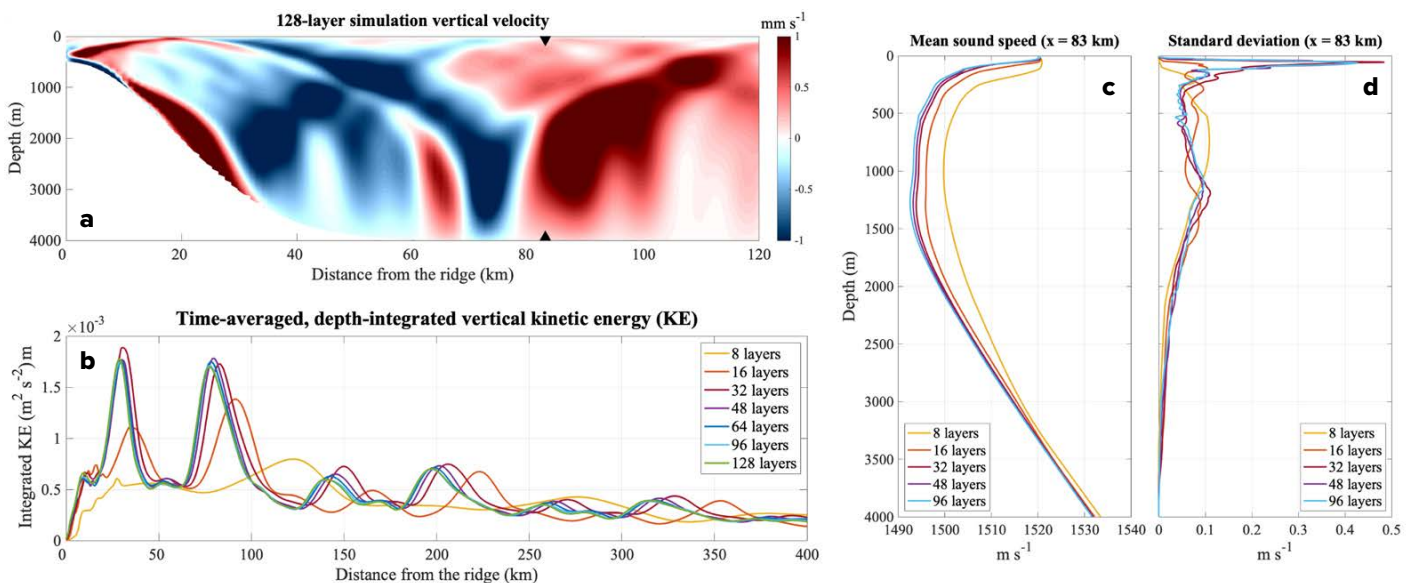


**FIGURE 4.** (a) Snapshot of the vertical velocity for the 128-layer simulation, zoomed in to the ridge centered at  $40^\circ\text{W}$ , where the domain is symmetric about the ridge. The black triangles indicate the location of the sound speed profiles in (c,d). (b) Time-averaged, depth-integrated vertical kinetic energy ( $\frac{1}{2} \int w^2 dz$ ), where  $w$  is the vertical velocity, for different vertical discretization: 8, 16, 32, 48, 64, 96, and 128 layers. (c) Mean and (d) standard deviation of sound speed 83 km from the ridge for the 8-, 16-, 32-, 48-, and 96-layer simulations.

studies considered IGW-IGW interactions to be the dominant processes. One mechanism, called “induced diffusion,” involves the interaction of near-inertial and tidal IGWs. Induced diffusion is thought to be very important in transferring KE across length scales. However, most studies have not considered IGW-eddy interactions in the same manner.

Skitka et al. (2024) used a framework to diagnose IGW-eddy interactions with IGW-IGW interactions in a regional MITgcm (1/48°) ocean simulation of the North Pacific. They found that IGW-eddy interactions induce a downscale KE flux in a manner analogous to IGW-IGW interactions. At this grid spacing, the “eddy-induced diffusion” was the dominant mechanism of energy exchange within the IGW supertidal continuum, and comparable to the wave-induced diffusion achieved by regional models with 250 m (1/192°) horizontal grid spacing. Thus, finer vertical and horizontal grid spacing is expected to change the details of the IGW cascade in simulations, including the mechanisms and rate of energy transfer and its dissipation.

## ACOUSTICS

### Tidally Forced Simulations and Sound Speed

We first examined how tidal forcing affects sound speed and acoustic properties using a series of global HYCOM (1/25°) simulations with or without tidal (T) forcing and with or without data assimilation (DA), four simulations in all. Each simulation was forced by wind and had 41 layers. Hourly output was recorded from May to June 2019. Temperature and salinity were interpolated from the native grid to a uniform 2 m vertical grid and then used to compute sound speed.

As an initial comparison, the sound speed variability in each of the four simulations was compared to glider observations over a small geographic area in the North Pacific (Figure 5a; Rudnick, 2016). A mean and standard deviation of sound speed was computed from May 20 to May 26, using three-hour output from the simulation and averaged over the region covered by the glider track. The glider profiled from the surface to 500 m depth roughly every three hours. Although this is not a region of large tidal energy, the simulations with tidal forcing still had

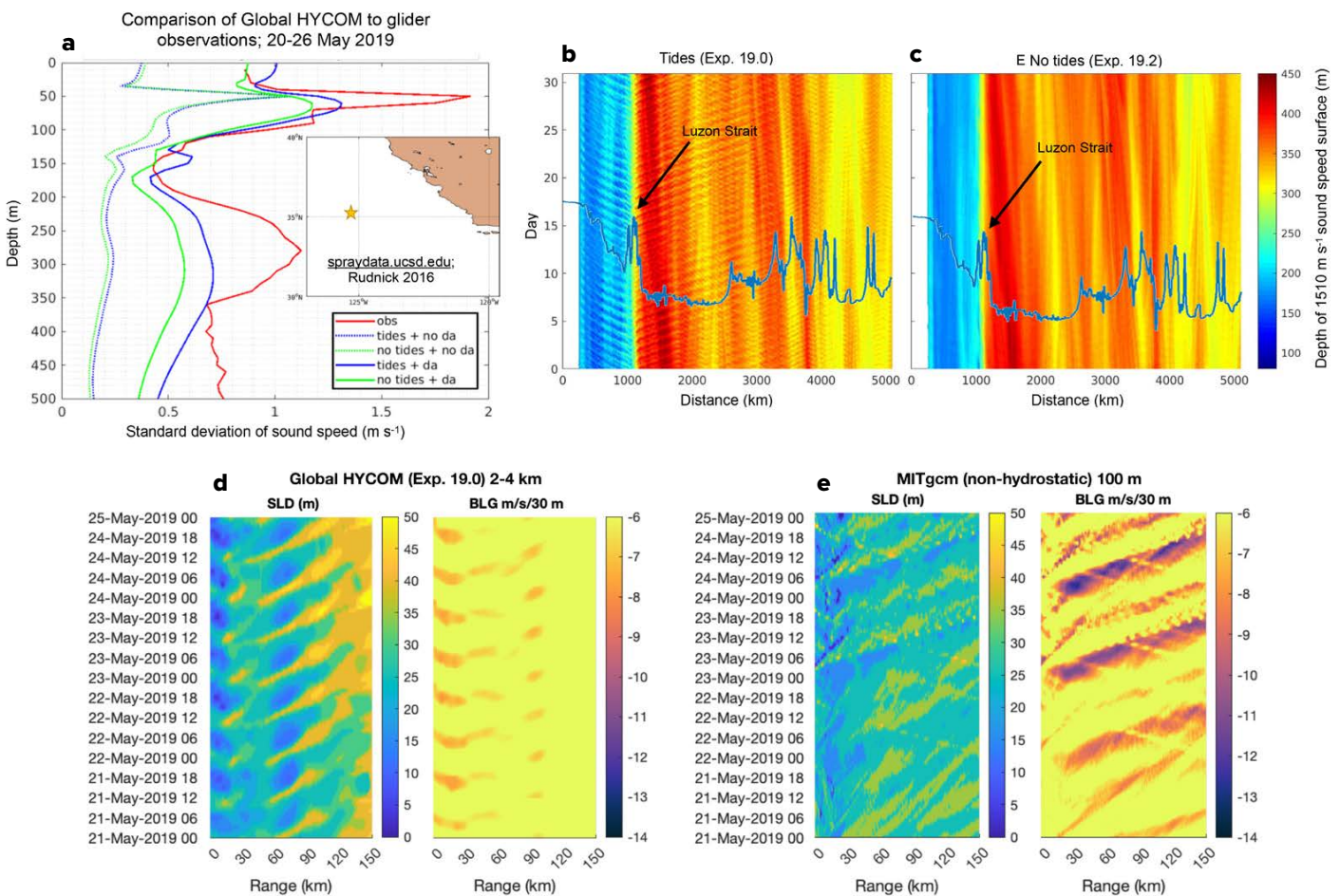


**FIGURE 5.** (a) Standard deviation of sound speed for May 20–26, 2019, from Global HYCOM simulations with and without tides and with and without data assimilation (DA) at the location indicated on the map off the coast of California. Simulations were compared to standard deviation computed from glider observations over the same week and location. (b,c) The depth of the 1510 m s<sup>-1</sup> sound speed along 20°N, extending from the coast of Hainan Island eastward (111.16°E–160°E) for global HYCOM simulations. Bathymetry is overlaid on each, with the Luzon Strait located at 1,000 km distance from the coast. (d,e) SLD and BLG for global HYCOM simulation with tides (Exp 19.0) and for a nonhydrostatic regional MITgcm simulation at the Mascarene Ridge near the island of Madagascar (see Figure 3b).

greater sound speed variability. A simulation with tidal forcing undulates the thermocline leading to greater temperature and salinity (and thus sound speed) variability at a given depth. Data assimilation brought the simulations closer to observations; however, it can also abruptly alter the temperature and salinity during an assimilation window, causing implausible jumps in sound speed. The elevated sound speed variability in the DA simulations could be caused by natural ocean variability or this “shock.” For these reasons, and those discussed in the earlier section, Internal Gravity Waves, we chose to use ocean simulations without DA while studying the sensitivity of acoustics to IGWs.

### Acoustic Case Studies at IGW Hotspots

At IGW hotspots, such as the Luzon Strait, the Amazon Shelf, and the Mascarene Ridge, tidal forcing strongly undulates the upper ocean, and there is IGW energy transfer among modes (see the section, From Global to Regional: Supertidal Energy). Across the Luzon Strait, we compared the depth variability of a single sound speed surface between the tidally forced and non-tidally forced global HYCOM simulations (Figure 5b,c). In the tidally forced simulation, depth striations radiated from the Luzon Ridge, located at 1,000 km distance, and other ridges with steep topography (e.g., 4,800 km) as tides propagated in both directions (Figure 5b). These were largely absent in the simulation without tides (Figure 5c).

We hypothesized that such differences in sound speed between the tidal and non-tidally forced simulations would cause notable differences in acoustic propagation. To test this idea, we turned to the Amazon region, where semidiurnal internal tides propagate northeastward away from the coast (Figure 3). The mean sound speed along the transect was similar between the tides and no-tides simulations (Figure 3g), but they differed in sound speed variability (Figure 3h). The tidal simulation had periodic “banding” in sound speed variability in the thermocline (~150 m depth) at locations near where there was greater IGW energy transfer (Figure 3a).

A 1,500 Hz virtual acoustic source was placed at 20 m depth at 4.1°N, 44.8°W, a location of enhanced sound speed variability and IGW energy transfer (yellow star in Figure 3a). The sound speed, vertical sound speed gradient, and transmission loss were examined along the 30° radial (clockwise from north). In the tidal case, there were undulations in sound speed and SLD (Figure 6a). Without tidal forcing, the sound speed was more uniform, and SLD was deeper. A deeper SLD will also typically improve transmission in the surface layer. Tidal forcing also introduced changes to vertical sound speed gradients (Figure 6a,b) and can be inferred to introduce them in the horizontal as well. Surface layer transmission occurred in both cases but was stronger in the simulation without tidal forcing. Turning to time series (Figure 6c), TL tended to be greater in simulations with tidal forcing than without and often fluctuated at semidiurnal timescales (i.e., every 12 hours), such as from May 20 to 23.

The semidiurnal variability extended to both SLD and BLG. In the nontidal case, TL varied with eddies and currents but not at semidiurnal frequencies (Figure 6c).

Because the horizontal and vertical structures of the sound speed determine the path of the sound, the introduction of vertical and horizontal gradients in sound speed in the simulation with tides could have resulted in more scattering and refraction of sound throughout the waveguide. However, the mesoscale differences between the tidal and non-tidal simulations made it difficult to directly compare their acoustic properties. Some of the simulation variability was caused by tidal interaction with the mesoscale field and atmospheric forcing. Correlation coefficients between wind and mixed layer depths in the Amazon region were similar between the tidally forced and non-tidal simulations, but with greater differences near the coast where currents and tidal variability were strongest.

### Sound Speed and Grid Spacing

Like IGWs, sound speed is also affected by simulation grid spacing. A finer grid may resolve more processes and have different temperature and salinity gradients. As an example, we compared two tidally forced simulations with different model setups to see how model grid-spacing and boundary conditions may affect sound speed structure: the hydrostatic tidally forced global HYCOM simulation (Experiment [Exp.] 19.0; 1/25° resolution; Figure 5d) and a two-dimensional nonhydrostatic simulation of the MITgcm (Figure 5e), with a horizontal grid spacing of 100 m. The Mascarene Ridge, where the simulations are compared, is known for nonlinear wave interactions; solitons are generated and propagate away from the ridge (Figure 3b,d,f). Because the simulations were initialized with an offset in temperature, they couldn't be compared directly; however, a relative comparison of SLD and BLG was insightful. The HYCOM simulation had organized semidiurnal fluctuations of the SLD and BLG, each oscillating twice a day (Figure 5d). In contrast, the MITgcm simulation had a periodic signal, but it appeared disorganized, with a more variable SLD and BLG (Figure 5e). The finer grid spacing of the MITgcm simulation likely allowed for nonlinear interactions to occur, which in turn impacted the sound speed structure. This structure is likely closer to real ocean variability, showing the difficulties of predicting sound speed using coarser-resolution ocean models.

To address the confounding challenges of the divergent mesoscale eddy fields and initialization states, we turned to the idealized model (section on Vertical Grid Spacing in Idealized Models) to isolate the impact of vertical grid spacing on sound speed. Hourly output from each of the idealized simulations with 8, 16, 32, 48, and 96 isopycnal layers was interpolated to a uniform depth coordinate for a 72-hour period. From this we calculated the sound speed means and standard deviations (Figure 4c,d). The mean sound speeds were greater in simulations with 32 or fewer layers (Figure 4c) and did not resolve

the depth of greatest sound speed variability (Figure 4d). As the number of layers increased, the mean and standard deviation of the sound-speed profiles converged, with very little difference between the 48- and 96-layer simulations. These results parallel the findings that, for a 1 km horizontal grid spacing, a minimum of 48 isopycnal layers is necessary to resolve displacement of isopycnals by internal tides.

## A DEEP LEARNING APPROACH TO INCLUDING IGW IN OCEAN MODELS

The finer grid spacing and the inclusion of tidal forcing in ocean simulations improves the realism of the ocean state. However, these improvements in a global ocean model are computationally

expensive. To reduce computational cost, we investigated using a generative adversarial network (GAN; Goodfellow et al., 2014) to generate a tidally forced ocean state without solving the physical forcing equations. GANs are a deep learning technique that learn a transformation from one statistical distribution to another instead of learning an exact distribution. In a GAN, a “generator,” which generates new data, is trained alongside a “discriminator,” which is a classifier that differentiates between actual data and generated data. The GAN works through iteration, with the generator learning a distribution transformation and the discriminator learning to distinguish between real data and generated data.

We trained two pairs of generators and discriminators using Global HYCOM (1/25°) with (Exp. 19.0) and without (Exp. 19.2)

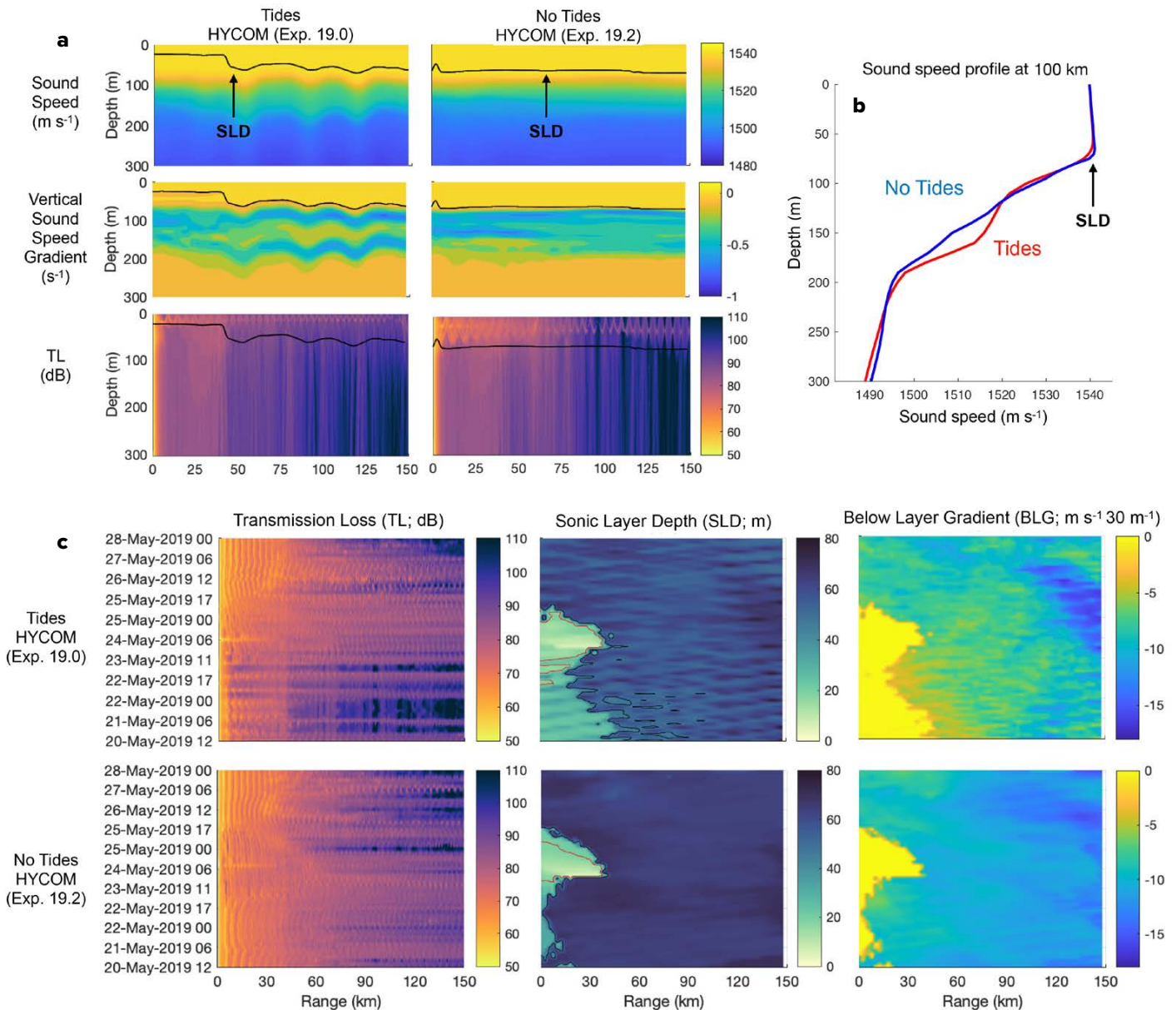


**FIGURE 6.** Comparison of acoustic propagation and properties between HYCOM simulations with and without tidal forcing at the Amazon Shelf, starting at 4.1°N, 44.8°W and extending 30° (clockwise from north) as indicated in Figure 3a. (a) A snapshot from May 20, 2019, 18:00:00 of sound speed (m s<sup>-1</sup>), vertical gradient of sound speed (s<sup>-1</sup>), and transmission loss (TL; dB) for each simulation. (b) A single sound speed profile at 100 km distance along the radial for the tidal (red) and non-tidal simulation. (c) TL at 20 m depth, sonic layer depth (SLD) and below-layer gradient (BLG). TL is calculated from a 1,500 Hz source at 4.1°N and 44.8°W at 20 m depth.

tidal forcing as the initialization states. One generator,  $G_{NT \rightarrow T}(\cdot)$ , translated from the non-tidal to the tidal domain, and the other generator,  $G_{T \rightarrow NT}(\cdot)$ , translated from the tidal to non-tidal domain. To address the issue of the chaotic, turbulent nature of the ocean, we considered the simulations to be unpaired (i.e., not a direct translation between one state and the other). Instead, the GAN used “cycle-consistency loss,” the mean-squared difference between the original data sample and the doubly translated data (Zhu et al., 2017). The cycle-consistency loss was combined with the traditional GAN losses (i.e., the difference between the generator and the discriminator output) to train the networks. The Atlantic Ocean was used as a test-case region; one week of hourly HYCOM data was split into 90% training data and 10% validation data.

The GAN results retained the general structure of the temperature and salinity profiles from HYCOM while adding or removing a semidiurnal tide (Figure 7). The GAN performed well in the relatively quiescent region of the tropical mid-Atlantic (Figure 7b). There, periodic signatures in HYCOM with tides matched the periodicity of the outputs of  $G_{NT \rightarrow T}(\cdot)$ . The

semidiurnal signature was also removed in  $G_{T \rightarrow NT}(\cdot)$  to match the non-tidally forced HYCOM. It was more difficult to separate the tidal structure from mesoscale variability in more energetic regions, such as near the Gulf Stream (Figure 7c,d). For example, just north of the Gulf Stream (Figure 7c), the  $G_{NT \rightarrow T}(\cdot)$  reproduced semidiurnal periodicity of the tidally forced HYCOM, but there was also periodicity in the nontidal fields. In the Gulf Stream extension (Figure 7d), the GAN imposed a periodicity to make the sample like other tidally forced results, but this was a region dominated by mesoscale variability.

Because the HYCOM output used to train the GAN was sampled from the same region of the globe during the same time of year, no two samples were completely independent. This introduces the risk of overfitting. Using unpaired data made the model more robust to overfitting but did not remove the risk entirely. Additionally, the sound speed structure had a persistent offset of about  $5 \text{ m s}^{-1}$  greater in the GAN-generated results than the original HYCOM simulations (not shown). Thus, although this work provides a good starting point, further work will help revise this approach.

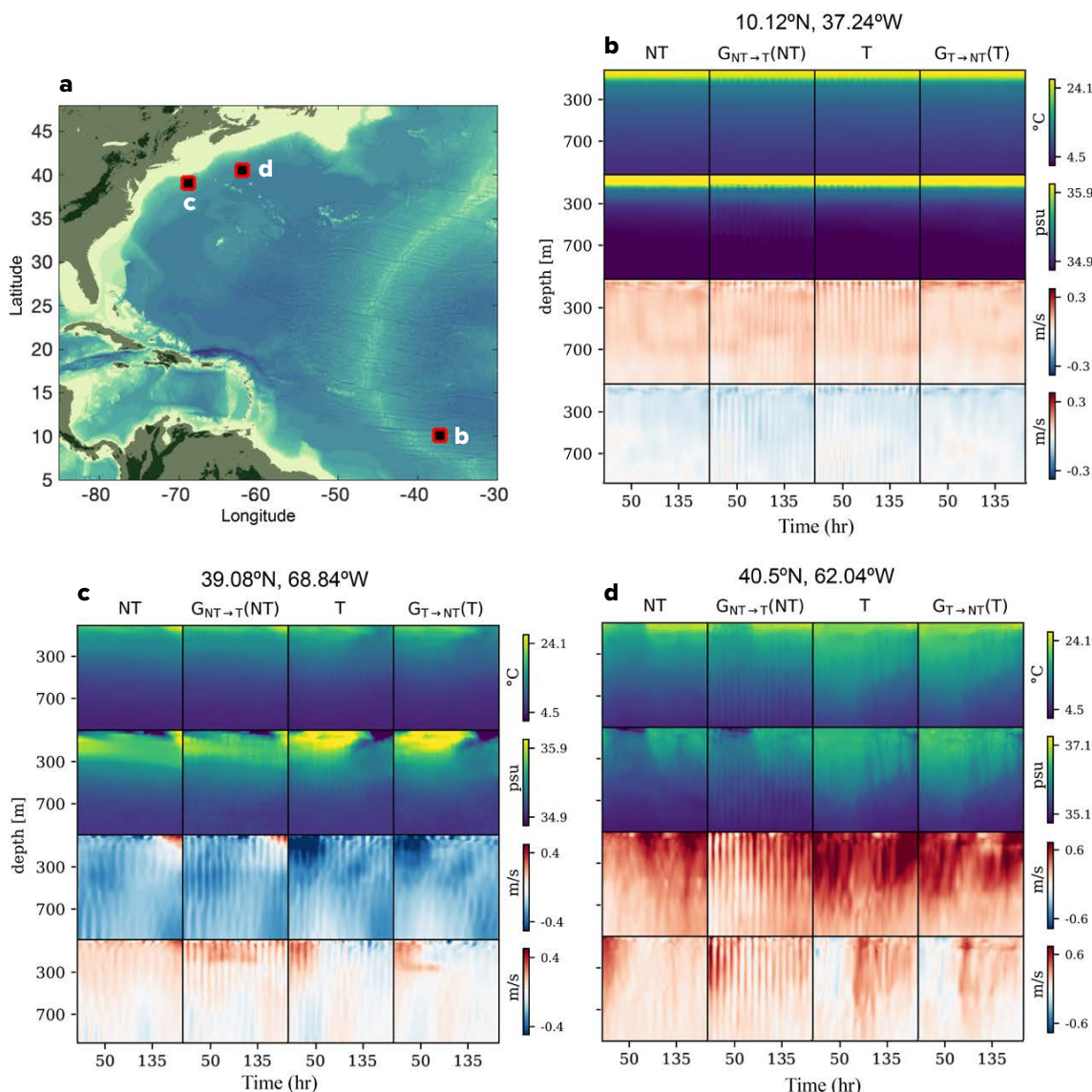


**FIGURE 7.** Temporal outputs of the deep learning GAN model at the locations mapped in (a). For each panel, the first column shows the non-tidal (NT) HYCOM results (Exp 19.2); the second column shows the NT results translated into the tidal domain using the GAN model; the third column shows the tidal (T) HYCOM results (Exp 19.0); and the fourth column shows the T results translated into the NT domain using a GAN model. From top to bottom, rows in (b–d) show water temperature, salinity, eastward velocity, and northward velocity, respectively.

## SUMMARY AND CONCLUSIONS

The TFO-HYCOM project was a cross-disciplinary investigation into the modeling of internal tides and high-frequency IGWS that explored their sensitivity to grid spacing, energy transfer, and dissipation; the impacts of tidal forcing in ocean simulations on sound speed structure and acoustic propagation; and the ability to use DL techniques to replicate tidally forced structure.

The inclusion of tidal forcing in global ocean models improved the representation of the ocean state and had a direct impact on sound speed at horizontal scales from kilometers to hundreds of kilometers and timescales on the order of a few to several hours. HYCOM simulations run with tides had greater sound-speed variance that was more consistent with observations. These impacts were sensitive to vertical and horizontal discretization, as were the ability of the simulations to resolve IGW interactions and energy transfer. Further investigations into the impacts of internal wave modeling choices on acoustic propagation could also be made by expanding acoustic frequency ranges, looking at acoustic arrival times, or comparing model results with observational studies. As running models at high resolution is computationally expensive, machine learning techniques may facilitate predictions of IGW impacts on ocean state in the future.

We have focused on the impacts of IGWs on sound; however, global ocean models are further used by stakeholders with diverse interests, such as the dispersal of biogeochemical tracers and biological productivity. As global operational models begin to include tidal forcing and incorporate finer grid spacing, it is important to understand how they represent physical processes and how energy cascades through the internal wave spectrum.

The ability to resolve IGWs in global ocean models has filter-down effects to several other fields such as ocean biological-physical interactions and ecosystem modeling. At shallow coastal locations, where biological productivity and freshwater input are large, the ability to resolve these IGW processes is important to understanding ecosystem dynamics. Among the range of their impacts, IGWs can alter distributions of organisms such as phytoplankton and chlorophyll, increase or decrease biological productivity, and alter predator-prey relationships (e.g., Evans et al., 2008; Lucas et al., 2011; Greer et al., 2014; Garwood et al., 2020). Having criteria for how IGWs can be resolved in a global model with a certain discretization will help interpret how well a model captures IGW energy transfer and the possible effects this may have on sound speed variability and ecosystem dynamics.

## REFERENCES

Ansong, J.K., B.K. Arbic, H.L. Simmons, M.H. Alford, M.C. Buijsman, P.G. Timko, and A.J. Wallcraft. 2018. Geographical distribution of diurnal and semidiurnal parametric subharmonic instability in a global ocean circulation model. *Journal of Physical Oceanography* 48:1409–1431, <https://doi.org/10.1175/JPO-D-17-0164.1>.

Arbic, B.K., S.T. Garner, R.W. Hallberg, and H.L. Simmons. 2004. The accuracy of surface elevations in forward global barotropic and baroclinic tide models. *Deep Sea Research Part II* 51:3,069–3,101, <https://doi.org/10.1016/j.dsr2.2004.09.014>.

Arbic, B.K., J.G. Richman, J.F. Shriver, P.G. Timko, E.J. Metzger, and A.J. Wallcraft. 2012. Global modeling of internal tides within an eddy ocean general circulation model. *Oceanography* 25(2):20–29, <https://doi.org/10.5670/oceanog.2012.38>.

Barkan, R., K.B. Winters, and J.C. McWilliams. 2017. Stimulated imbalance and the enhancement of eddy kinetic energy dissipation by internal waves. *Journal of Physical Oceanography* 47(1):181–198, <https://doi.org/10.1175/JPO-D-16-0117.1>.

Bell, T.H. Jr. 1975. Topographically generated internal waves in the open ocean. *Journal of Geophysical Research* 80(3):320–327, <https://doi.org/10.1029/JC080i003p00320>.

Bleck, R. 2002. An oceanic general circulation model framed in hybrid isopycnic-Cartesian coordinates. *Ocean Modelling* 4:55–88, [https://doi.org/10.1016/S1463-5003\(01\)00012-9](https://doi.org/10.1016/S1463-5003(01)00012-9).

Buijsman, M., G.R. Stephenson, J.K. Ansong, B.K. Arbic, M. Green, J.G. Richman, J.F. Shriver, C. Vic, A.J. Wallcraft, and Z. Zhao. 2020. On the interplay between horizontal resolution and wave drag and their effect on tidal baroclinic mode waves in realistic global ocean simulations. *Ocean Modelling* 152:101656, <https://doi.org/10.1016/j.ocemod.2020.101656>.

Buijsman, M.C., M.A. Abdulfatai, B.K. Arbic, E.P. Chassignet, L. Hiron, J.F. Shriver, M. Solano, D. Varma, and X. Xu. 2025. Energetics of (super)tidal baroclinic modes in a realistically forced global ocean simulation. *ESS Open Archive*, <https://doi.org/10.22541/essoar.173939615.50210043/v1>.

Chassignet, E.P., H.E. Hurlburt, O.M. Smedstad, G.R. Halliwell, A.J. Wallcraft, E.J. Metzger, B.O. Blanton, C. Lozano, D.B. Rao, P.J. Hogan, and A. Srinivasan. 2006. Generalized vertical coordinates for eddy-resolving global and coastal ocean forecasts. *Oceanography* 19(1):118–129, <https://doi.org/10.5670/oceanog.2006.95>.

Chassignet, E.P., and X. Xu. 2017. Impact of horizontal resolution (1/12° to 1/50°) on Gulf Stream separation, penetration, and variability. *Journal of Physical Oceanography* 47:1,999–2,021, <https://doi.org/10.1175/JPO-D-17-0031.1>.

Colosi, J.A., and S.M. Flatté. 1996. Mode coupling by internal waves for multimegahertz acoustic propagation in the ocean. *Journal of the Acoustical Society of America* 100(6):3,607–3,620, <https://doi.org/10.1121/1.417334>.

Dematteis, G., K. Polzin, and Y.V. Lvov. 2022. On the origins of the oceanic ultraviolet catastrophe. *Journal of Physical Oceanography* 52(4):597–616, <https://doi.org/10.1175/JPO-D-21-0121.1>.

Dushaw, B.D. 2022. Surprises in physical oceanography: Contributions from ocean acoustic tomography. *Tellus A* 74(1):33–67, <https://doi.org/10.16993/tellusa.39>.

Dzieciuch, M., W. Munk, and D.L. Rudnick. 2004. Propagation of sound through a spicy ocean, the SOFAR overtone. *Journal of the Acoustical Society of America* 116(3):1,447–1,462, <https://doi.org/10.1121/1.1772397>.

Evans, M.A., S. MacIntyre, and G.W. Kling. 2008. Internal wave effects on photosynthesis: Experiments, theory, and modeling. *Limnology and Oceanography* 53(1):339–353, <https://doi.org/10.4319/lo.2008.53.1.0339>.

Flatté, S.M., R. Dashen, W. Munk, K. Watson, and F. Zachariassen. 1979. *Sound Transmission Through a Fluctuating Ocean*. Cambridge University Press, Cambridge, UK, 320 pp.

Garrett, C., and W. Munk. 1975. Space-time scales of internal waves: A progress report. *Journal of Geophysical Research* 80(3):291–297, <https://doi.org/10.1029/JC080i003p00291>.

Garrett, C., and E. Kunze. 2007. Internal tide generation in the deep ocean. *Annual Review of Fluid Mechanics* 39(1):57–87, <https://doi.org/10.1146/annurev.fluid.39.050905.110227>.

Garwood, J.C., R.C. Musgrave, and A.J. Lucas. 2020. Life in internal waves. *Oceanography* 33(3):38–49, <https://doi.org/10.5670/oceanog.2020.313>.

Gill, A.E. 1982. *Atmosphere-Ocean Dynamics*. International Geophysics Series, vol. 30, Academic Press, London, UK, 680 pp.

Goodfellow, I.J., J. Pouget-Abadie, M. Mirza, B. Xu, D. Warde-Farley, S. Ozair, A. Courville, and Y. Bengio. 2014. Generative adversarial networks. *ArXiv:1406.2661 [Cs, Stat]*, <https://doi.org/10.48550/arXiv.1406.2661>.

Greer, A., R.K. Cowen, C.M. Guigand, J.A. Hare, and D. Tang. 2014. The role of internal waves in larval fish interactions with potential predators and prey. *Progress in Oceanography* 127:47–61, <https://doi.org/10.1016/j.pocan.2014.05.010>.

Helber, R.W., C.N. Barron, M.R. Carnes, and R.A. Zingarelli. 2008. Evaluating the sonic layer depth relative to the mixed layer depth. *Journal of Geophysical Research* 113(C7), <https://doi.org/10.1029/2007JC004595>.

Hendershott, M.C. 1981. Long waves and ocean tides. Pp. 292–341 in *Evolution of Physical Oceanography*. B. Warren and C. Wunsch, eds, MIT Press.

Hiron, L., M.C. Schönau, K.J. Raja, E.P. Chassignet, M.C. Buijsman, B.K. Arbic, A. Bozec, E.F. Coelho, and M.S. Solano. 2025. The influence of vertical resolution on internal tide energetics and subsequent effects on underwater acoustic propagation. *Journal of Advances in Modeling Earth Systems* 17:e2024MS004389, <https://doi.org/10.1029/2024MS004389>.

Hogan, T.F., M. Liu, J.A. Ridout, M.S. Peng, T.R. Whitcomb, B.C. Ruston, C.A. Reynolds, S.D. Eckermann, J.R. Moskaitis, N.L. Baker, and others. 2014. The Navy Global Environmental Model. *Oceanography* 27(3):116–125, <https://doi.org/10.5670/oceanog.2014.73>.

Lucas, A.J., P.J.S. Franks, and C.L. Dupont. 2011. Horizontal internal-tide fluxes support elevated phytoplankton productivity over the inner continental shelf. *Limnology and Oceanography: Fluids and Environments* 1(1):56–74, <https://doi.org/10.1215/21573698-1258185>.

MacKinnon, J.A., Z. Zhao, C.B. Whalen, A.F. Waterhouse, D.S. Trossman, O.M. Sun, L.C. St. Laurent, H.L. Simmons, K. Polzin, R. Pinkel, and others. 2017. Climate Process Team on Internal Wave–Driven Ocean Mixing. *Bulletin of the American Meteorological Society* 98(11):2,429–2,454, <https://doi.org/10.1175/BAMS-D-16-0030.1>.

Metzger, E.J., O.M. Smedstad, P.G. Thoppil, H.E. Hurlburt, J.A. Cummings, A.J. Wallcraft, L. Zamudio, D.S. Franklin, P.G. Posey, M.W. Phelps, and others. 2014. US Navy operational global ocean and Arctic ice prediction systems. *Oceanography* 27(3):32–43, <https://doi.org/10.5670/oceanog.2014.66>.

McComas, C.H., and F.P. Bretherton. 1977. Resonant interaction of oceanic internal waves. *Journal of Geophysical Research* 82(9):1,397–1,412, <https://doi.org/10.1029/JC082i009p01397>.

Müller, P., G. Holloway, F. Henyey, and N. Pomphrey. 1986. Nonlinear interactions among internal gravity waves. *Reviews of Geophysics* 24(3):493–536, <https://doi.org/10.1029/RG024i003p00493>.

Ngodock, H.E., I. Souppgui, A.J. Wallcraft, J.G. Richman, J.F. Shriver, and B.K. Arbic. 2016. On improving the accuracy of the barotropic tides embedded in a high-resolution global ocean circulation model. *Ocean Modelling* 97:16–26, <https://doi.org/10.1016/j.ocemod.2015.10.011>.

Pollard, R.T., and R.C. Millard. 1970. Comparison between observed and simulated wind-generated inertial oscillations. *Deep Sea Research and Oceanographic Abstracts* 17(4):813–821, [https://doi.org/10.1016/0011-7471\(70\)90043-4](https://doi.org/10.1016/0011-7471(70)90043-4).

Porter, M.B. 2011. The BELLHOP Manual and User's Guide: PRELIMINARY DRAFT. Heat, Light, and Research Inc., La Jolla, California, <http://oalib.hlsresearch.com/Rays/HLS-2010-1.pdf>.

Raja, K.J., M.C. Buijsman, J.F. Shriver, B.K. Arbic and O. Siyanbola. 2022. Near-inertial wave energetics modulated by background flows in a global model simulation. *Journal of Physical Oceanography* 52(5):823–840, <https://doi.org/10.1175/JPO-D-21-0130.1>.

Raja, K.J., M.C. Buijsman, A. Bozec, R.W. Helber, J.F. Shriver, A. Wallcraft, E.P. Chassignet, and B.K. Arbic. 2024. Spurious internal wave generation during data assimilation in eddy resolving ocean model simulations. *Ocean Modelling* 188:102340, <https://doi.org/10.1016/j.ocemod.2024.102340>.

Rudnick, D. 2016. California Underwater Glider Network [Data set]. Scripps Institution of Oceanography, Instrument Development Group, <https://doi.org/10.21238/S8SPRAY1618>.

Simmons, H.L., R.W. Hallberg, and B.K. Arbic. 2004. Internal wave generation in a global baroclinic tide model. *Deep Sea Research Part II* 51:3,043–3,068, <https://doi.org/10.1016/j.dsr2.2004.09.015>.

Skitka, J., B.K. Arbic, R. Thakur, D. Menemenlis, W.R. Peltier, Y. Pan, K. Momeni, and Y. Ma. 2024. Probing the nonlinear interactions of superinertial internal waves using a high-resolution regional ocean model. *Journal of Physical Oceanography* 54(2):399–425, <https://doi.org/10.1175/JPO-D-22-0236.1>.

Solano, M., M.C. Buijsman, J.F. Shriver, J. Magalhaes, J.C. Da Silva, C. Jackson, B.K. Arbic, and R. Barkan. 2023. Nonlinear internal tides in a realistically forced global ocean simulation. *Journal of Geophysical Research* 128:e2023JC019913, <https://doi.org/10.1029/2023JC019913>.

Stewart, K.D., A.McC. Hogg, S.M. Griffies, A.P. Heerdegen, M.L. Ward, P. Spence, and M.H. England. 2017. Vertical resolution of baroclinic modes in global ocean models. *Ocean Modelling* 113:50–65, <https://doi.org/10.1016/j.ocemod.2017.03.012>.

Tang, D., J.N. Moum, J.F. Lynch, P. Abbot, R. Chapman, P.H. Dahl, T.F. Duda, G. Gawarkiewicz, S. Glenn, J.A. Goff, and others. 2007. Shallow Water '06: A joint acoustic propagation/nonlinear internal wave physics experiment. *Oceanography* 20(4):156–167, <https://doi.org/10.5670/oceanog.2007.16>.

Worcester, P.F., M.A. Dzieciuch, J.A., Mercer, R.K. Andrew, B.D. Dushaw, A.B. Baggeroer, K.D. Heaney, G.L. D'Spain, J.A. Colosi, R.A. Stephen, and others. 2013. The North Pacific Acoustic Laboratory deep-water acoustic propagation experiments in the Philippine Sea. *Journal of the Acoustical Society of America* 134:3,359–3,375, <https://doi.org/10.1121/1.4818887>.

Xu, X., E.P. Chassignet, A.J. Wallcraft, B.K. Arbic, M.C. Buijsman, and M. Solano. 2022. On the spatial variability of the mesoscale sea surface height wavenumber spectra in the Atlantic Ocean. *Journal of Geophysical Research: Oceans* 127:e2022JC018769, <https://doi.org/10.1029/2022JC018769>.

Zhou, X.-H., D.-P. Wang, and D. Chen. 2015. Global wavenumber spectrum with corrections for altimeter high frequency noise. *Journal of Physical Oceanography* 45(2):495–503, <https://doi.org/10.1175/JPO-D-14-0144.1>.

Zhu, J.Y., T. Park, P. Isola, and A.A. Efros. 2017. Unpaired image-to-image translation using cycle-consistent adversarial networks. Pp. 2,223–2,232 in *Proceedings of the IEEE International Conference on Computer Vision*, Venice, Italy, October 22–29, 2017, <https://doi.org/10.1109/ICCV.2017.244>.

## ACKNOWLEDGMENTS

This TFO-HYCOM project was funded by related Office of Naval Research (ONR) grants to the different institutions involved: N00014-19-1-2712 to University of Michigan, N00014-19-1-2717 to Florida State University, N00014-19-1-2704 to University of Southern Mississippi, N00014-20-C-2018 to ARIA and Applied Ocean

Sciences LLC, and contract number N00014-22WX00941 to the Naval Research Laboratory. We gratefully acknowledge ONR for support of our research and thank the reviewers of this article for their helpful suggestions and insights.

## AUTHOR CONTRIBUTIONS

This manuscript highlights the research efforts by postdocs and early career researchers on the TFO-HYCOM project. The team was guided by senior scientist co-PIs at each institution. J. Summers served as lead principal investigator. B. Arbic conceived the idea of a project and organized regular group meetings. The team that focused on improving IGW modeling was composed of researchers from the Naval Research Laboratory (NRL), Florida State University (FSU), University of Southern Mississippi (USM), and University of Michigan (U-M). The NRL team provided 1/25° global HYCOM simulations. FSU researchers performed 1/50° North Atlantic basin simulations and idealized simulations. USM researchers examined IGW modes and KE transfer and provided MITgcm simulations along the Mascarene Ridge, while U-M researchers examined the theory of IGW non-linear energy transfer and dissipation in high-resolution regional MITgcm simulations. Researchers from NRL and Applied Ocean Sciences assessed acoustics, and researchers from Applied Research in Acoustics LLC applied deep learning algorithms. Figures were contributed as follows: 3g–h, 5d–e, 6, and 7a (Schönau); 4 (Hiron); 7b–d (Ragland and Peria); 2a–b and 3a–f (Solano); 1 (Xu); 5a–c (Shriver and Helber); 2c (Buijsman).

## AUTHORS

**Martha C. Schönau** ([mschonau@ucsd.edu](mailto:mschonau@ucsd.edu)), formerly at Applied Ocean Sciences (AOS), now at Scripps Institution of Oceanography, University of California, San Diego, La Jolla, CA, USA. **Luna Hiron**, Center for Ocean-Atmospheric Prediction Studies, Florida State University, Tallahassee, FL, USA. **John Ragland**, Applied Research in Acoustics LLC (ARIA) and Department of Electrical and Computer Engineering, University of Washington, Seattle, WA, USA. **Keshav J. Raja**, Center for Ocean-Atmospheric Prediction Studies, Florida State University, Tallahassee, FL, USA. **Joseph Skitka**, formerly in the Department of Earth and Environmental Sciences, University of Michigan, Ann Arbor, MI, USA, now in the Department of Physical Oceanography, Woods Hole Oceanographic Institution, Woods Hole, MA, USA. **Miguel S. Solano**, formerly in the School of Ocean Science and Engineering, The University of Southern Mississippi, Hattiesburg, MS, USA, now at Sofar Ocean Technologies, San Francisco, CA, USA. **Xiaobiao Xu**, Center for Ocean-Atmospheric Prediction Studies, Florida State University, Tallahassee, FL, USA. **Brian K. Arbic**, Department of Earth and Environmental Sciences, University of Michigan, Ann Arbor, MI, USA. **Maarten C. Buijsman**, School of Ocean Science and Engineering, The University of Southern Mississippi, Hattiesburg, MS, USA. **Eric P. Chassignet**, Center for Ocean-Atmospheric Prediction Studies, Florida State University, Tallahassee, FL, USA. **Emanuel Coelho**, AOS, Arlington, VA, USA. **Robert W. Helber**, Naval Research Laboratory, Ocean Dynamics and Prediction, Stennis Space Center, MS, USA. **William Peria**, ARIA, Seattle, WA, USA. **Jay F. Shriver**, Naval Research Laboratory, Ocean Dynamics and Prediction, Stennis Space Center, MS, USA. **Jason E. Summers**, ARIA, Seattle, WA, USA. **Kathryn L. Verlinden**, AOS, Portland, OR, USA. **Alan J. Wallcraft**, Center for Ocean-Atmospheric Prediction Studies, Florida State University, Tallahassee, FL, USA.

## ARTICLE CITATION

Schönau, M.C., L. Hiron, J. Ragland, K.J. Raja, J. Skitka, M.S. Solano, X. Xu, B.K. Arbic, M.C. Buijsman, E.P. Chassignet, E. Coelho, R.W. Helber, W. Peria, J.F. Shriver, J.E. Summers, K.L. Verlinden, and A.J. Wallcraft. 2025. How do tides affect underwater acoustic propagation? A collaborative approach to improve internal wave modeling at basin to global scales. *Oceanography* 38(2), <https://doi.org/10.5670/oceanog.2025.308>.

## COPYRIGHT & USAGE

This is an open access article made available under the terms of the Creative Commons Attribution 4.0 International License (<https://creativecommons.org/licenses/by/4.0/>), which permits use, sharing, adaptation, distribution, and reproduction in any medium or format as long as users cite the materials appropriately, provide a link to the Creative Commons license, and indicate the changes that were made to the original content.